nature physics

Supplementary information https://doi.org/10.1038/s41567-024-02708-5

Thermally driven quantum refrigerator autonomously resets a superconducting qubit

In the format provided by the authors and unedited

Supplementary Information: Thermally driven quantum refrigerator autonomously resets superconducting qubit

Mohammed Ali Aamir,[1,*] Paul Jamet Suria,[1] José Antonio Marín Guzmán,[2] Claudia Castillo-Moreno,[1] Jeffrey M. Epstein,[2,3] Nicole Yunger Halpern,[2,3,†] and Simone Gasparinetti[1,‡]

[1]*Department of Microtechnology and Nanoscience, Chalmers University of Technology, 412 96 Gothenburg, Sweden*
[2]*Joint Center for Quantum Information and Computer Science, NIST and University of Maryland, College Park, MD 20742, USA*
[3]*Institute for Physical Science and Technology, University of Maryland, College Park, MD 20742, USA*

CONTENTS

* aamir.ali@chalmers.se
† nicoleyh@umd.edu
‡ simoneg@chalmers.se

I. FULL EXPERIMENTAL SETUP AND PARAMETERS

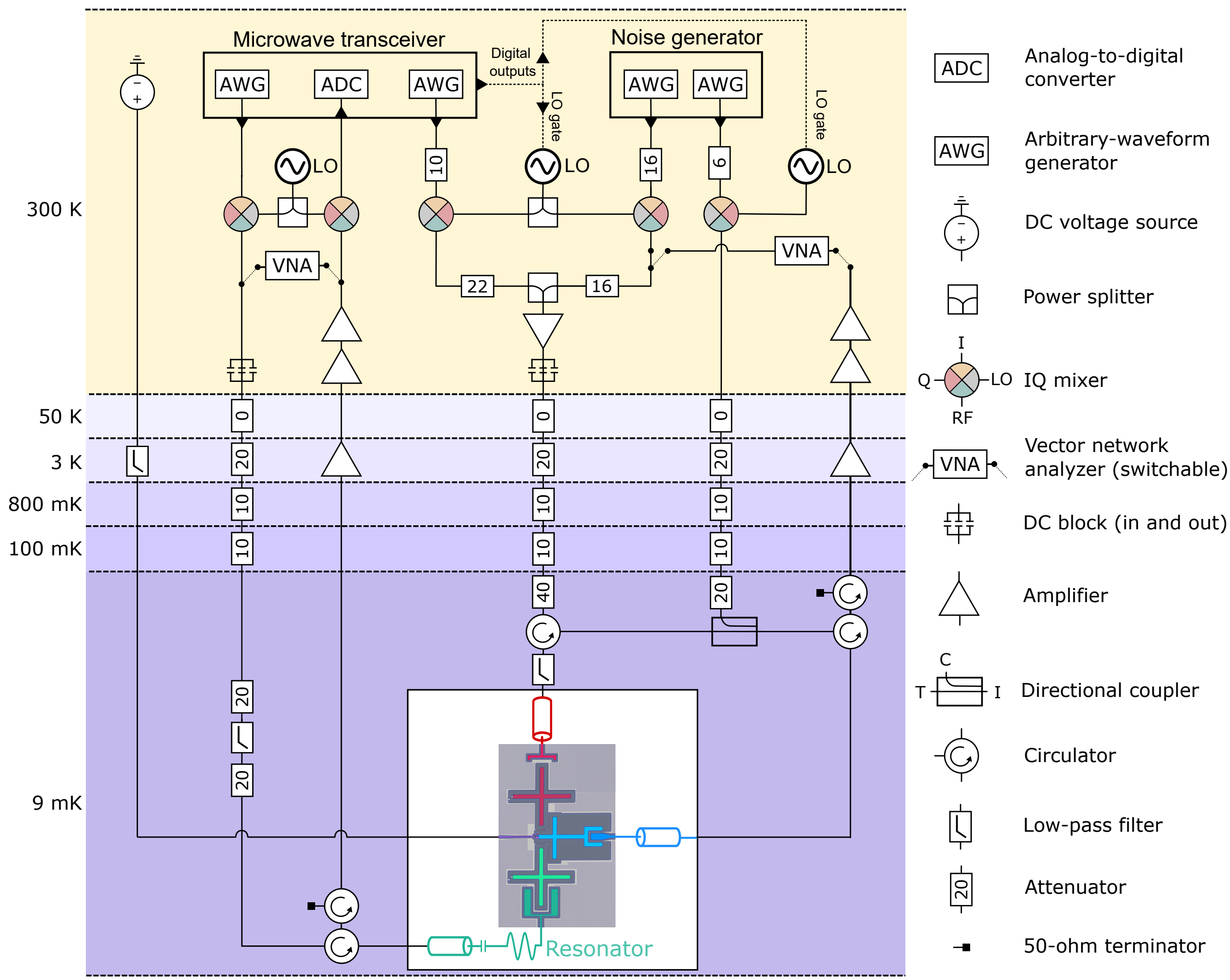

FIG. S1: Complete experimental set-up. See text for description. The in-phase-quadrature (IQ) mixers' ports, I and Q, are both used to connect to the microwave transceiver. However, only port I is shown to be wired; port Q is omitted for clarity. Digital outputs from the microwave transceiver are used to gate the local oscillators (LO) to produce pulses of thermal microwave modes. The directional coupler has 3 ports, called the input port (I), coupled port (C), and through port (T).

Figure S1 shows a schematic of the experimental set-up used to study our quantum absorption refrigerator (QAR). The QAR is packaged in a copper enclosure and mounted on the mixing-chamber stage of a dilution refrigerator that reaches 10 mK. The QAR is packaged in multiple layers: two nested copper enclosures shield the QAR from electromagnetic waves. A μ-metal enclosure protects the QAR from low-frequency magnetic fields. Microwave fields (both coherent and thermal) are routed to the QAR through highly attenuated input coaxial lines. The outgoing fields are routed through the output lines and are boosted by a cryogenic high-electron-mobility transistor (HEMT) amplifier (provided by Low Noise Factory) at 3 K and by room-temperature amplifiers. Microwave circulators separate the input and output signals. The resonator, dispersively coupled to qubit Q_3, is probed by a microwave feedline in reflection mode. We probe and drive Q_1 and Q_2, via the waveguide coupled to each, using two attenuated coaxial lines. We use a microwave directional coupler with three ports (input port, coupled port, and through port). Their arrangement allows us to use one output line for both Q_1's and Q_2's waveguides, taking advantage of the relevant transitions' nonoverlapping frequencies. Specifically, we combine the outgoing field from Q_1 (entering the through port) with the incoming field (entering the coupled port) intended for Q_2. The resultant field (exiting from the input port of the directional coupler) is routed by a circulator to Q_2's waveguide.

Parameter	Symbol	Value
Q_1 mode frequency	$\omega_1/(2\pi)$	5.327 GHz
Q_2 mode-tunable frequency range	$\omega_2/(2\pi)$	4.2 GHz to 4.9 GHz
Q_2 resonant frequency	$\omega_2^{\text{res}}/(2\pi)$	4.629 GHz
Q_3 mode frequency	$\omega_3/(2\pi)$	3.725 GHz
Q_1 anharmonicity	$\alpha_1/(2\pi)$	-213.4 MHz
Q_2 anharmonicity	$\alpha_2/(2\pi)$	-205.1 MHz
Q_3 anharmonicity	$\alpha_3/(2\pi)$	-237.8 MHz
Q_1 radiative-emission rate	$\Gamma_1/(2\pi)$	70 kHz
Q_2 radiative-emission rate	$\Gamma_2/(2\pi)$	7.2 MHz
Q_3 natural energy-relaxation time	T_{relax}	16.8 μs
Three-body-coupling rate	$A/(2\pi)$	3.2 MHz

TABLE S1: Experimentally measured parameters' values.

We use a microwave transceiver (Vivace from Intermodulation Products, Sweden), with in-phase-quadrature (IQ) mixers and local oscillators (LO), for driving the qudits and for readout measurements of Q_3. The physical connections can be switched to a vector network analyzer (VNA). The VNA is used for continuous-wave spectroscopy that allows for basic characterization, e.g., of a qudit's frequency and anharmonicity.

The waveguide coupled to Q_1 is populated with synthesized thermal microwave modes limited to a 50 MHz bandwidth centered at the qubit's frequency. An analogous statement concerns the waveguide coupled to Q_2. To populate the waveguides, we first continuously generate voltage noise with a white (flat) spectral density, using an arbitrary-waveform generator (AWG) limited to a 50 MHz bandwidth centered at a frequency of 100 MHz. The equipment used is a Keysight 3202A, which is limited to a 500 MHz bandwidth. Next, the generated noise is up-converted with IQ mixers and microwave tones ($\approx$ 4 GHz to 6 GHz) generated by an LO. Finally, the resulting continuous thermal radiation is chopped into pulses synchronized with Q_3-state readouts (see Fig. 3 in the main text). This process is performed via modulation (gating) of the LO outputs (Anapico APMS20G-4-ULN), with help from the transceiver's digital logic outputs, over time intervals of 10 ns and longer. To characterize the qudits (e.g., to determine their frequencies), we can switch the input/output lines to VNA. Furthermore, to observe the three-body interactions with coherent drives (see Fig. 2 in the main text), we can switch qubit Q_1's input line to the transceiver's AWG[1]. Table S1 shows the QAR's experimentally inferred parameters.

II. THEORETICAL MODEL

The Hamiltonian of our QAR's three-qudit system can be written as

$$\hat{H} = \sum_{i=1}^{3} \left(\tilde{\omega}_i \hat{a}_i^\dagger \hat{a}_i + \alpha_i \hat{a}_i^\dagger \hat{a}_i^\dagger \hat{a}_i \hat{a}_i / 2 \right) + g_{12} \left(\hat{a}_1^\dagger \hat{a}_2 + \hat{a}_1 \hat{a}_2^\dagger \right) + g_{23} \left(\hat{a}_2^\dagger \hat{a}_3 + \hat{a}_2 \hat{a}_3^\dagger \right) . \tag{S1}$$

$\hat{a}_i$ and $\hat{a}_i^\dagger$ denote qudit Q_i's annihilation and creation operators. $\tilde{\omega}_i$ and α_i denote qudit Q_i's bare mode frequency and anharmonicity. g_{12} (g_{23}) denotes the rate of the coupling between qudits Q_1 and Q_2 (qudits Q_2 and Q_3).

We engineer an effective three-body interaction by meeting the resonance condition $\omega_1 + \omega_3 = 2\omega_2 + \alpha_2$ and using Josephson junctions that facilitate the four-wave mixing [1]. The three-body interaction interchanges the three-qudit states $|101\rangle$ and $|020\rangle$ (see the notation and Fig. 1c in the main text).

We now introduce an approximation to $\hat{H}$. Denote by A the rate at which $|101\rangle$ and $|020\rangle$ couple coherently. $\hat{H}$ is well-approximated by the effective Hamiltonian

$$\hat{H}_{\text{eff}} = \sum_{i=1}^{3} \omega_i \hat{a}_i^\dagger \hat{a}_i + \sum_{i,j=1}^{3} \frac{\alpha_{ij}}{2} \hat{a}_i^\dagger \hat{a}_i \hat{a}_j^\dagger \hat{a}_j + A \left(|101\rangle\langle 020| + |020\rangle\langle 101| \right) . \tag{S2}$$

[1] Certain equipment, instruments, software, or materials are identified in this paper to specify the experimental procedure adequately. Such identification is not intended to imply the recommendation or endorsement of any product or service by NIST; nor is it intended to imply that the materials or equipment identified are necessarily the best available for the purpose.

The simplification follows from black-box quantization [2] and second-order time-independent perturbation theory [1]. H_{eff} depends on dressed modes associated with annihilation and creation operators $\hat{a}_i$ and $\hat{a}_i^\dagger$, dressed-mode frequencies ω_i, and self-Kerr and cross-Kerr coupling rates α_{ij}.

Let us introduce into the model a drive, as shown in Fig. 2 of the main text. This coherent drive is applied to Q_1 at the drive frequency ω_{d} and the rate Ω. Upon adding a drive term to $\hat{H}_{\text{eff}}$, we apply the rotating-wave approximation. We obtain the full Hamiltonian

$$\hat{H}_{\text{D1}} = \sum_{i=1}^{3} \delta_i \hat{a}_i^\dagger \hat{a}_i + \sum_{i,j=1}^{3} \frac{\alpha_{ij}}{2} \hat{a}_i^\dagger \hat{a}_i \hat{a}_j^\dagger \hat{a}_j + A\left(|101\rangle\langle 020| + |020\rangle\langle 101|\right) + \frac{\Omega}{2}\left(\hat{\hat{a}}_1 + \hat{\hat{a}}_1^\dagger\right). \tag{S3}$$

The effective frequency $\delta_i \coloneqq \omega_d - \omega_i$.

To model the measurements of Fig. 2, we solve a Lindblad quantum master equation:

$$\frac{\partial \hat{\rho}}{\partial t} = -\frac{i}{\hbar}[\hat{H}_{D1}, \rho] + \sum_{i=1}^{3} \Gamma_i \mathcal{D}[\hat{\hat{a}}_i, \rho]. \tag{S4}$$

We model the waveguides as zero-temperature baths (with average occupation numbers of 0). The qudits can interact with such baths just through spontaneous emission [3]. We have suppressed the time dependence of ρ in our notation. At all times t, ρ approximately equals the tensor product of the qudits' reduced states, ρ_i: $\rho = \rho_1 \otimes \rho_2 \otimes \rho_3$. $\Gamma_{i=1,2}$ denotes the rate at which qudit Q_i couples to its waveguide. Γ_E, Q_3's natural energy-relaxation rate, is related to the qubit's energy-relaxation time T_{relax} when refrigerator is inactive through $\Gamma_E = 1/T_{\text{relax}}$. The dissipator superoperator $\mathcal{D}$ is defined through

$$\mathcal{D}[\hat{A}, \hat{B}] = \hat{A}\hat{B}\hat{A}^\dagger - \frac{1}{2}\left(\hat{A}^\dagger \hat{A}\hat{B} + \hat{B}\hat{A}^\dagger \hat{A}\right), \tag{S5}$$

for operators $\hat{A}$ and $\hat{B}$.

To model the QAR interacting with two heat baths, we limit our analysis to a subspace of the full Hilbert space. This subspace is spanned by the basis $\mathcal{B} = \{|000\rangle, |100\rangle, |010\rangle, |001\rangle, |002\rangle, |102\rangle, |020\rangle, |101\rangle\}$ containing 8 levels. The population of $|i\rangle \in \mathcal{B}$ is $p_i \coloneqq \rho_{ii} \coloneqq \langle i|\hat{\rho}|i\rangle$. We formulate an 8-level population-rate model to calculate these populations's dynamics. To capture the coherent exchanges between $|101\rangle$ and $|020\rangle$, we also include an off-diagonal element $\rho_{\text{coh}} = \langle 101|\hat{\rho}|020\rangle$ in the model. Combining these ingredients, we introduce the rate equation for the populations:

$$\frac{d}{dt}\begin{pmatrix} p_{|000\rangle}(t) \\ p_{|100\rangle}(t) \\ p_{|010\rangle}(t) \\ p_{|001\rangle}(t) \\ p_{|002\rangle}(t) \\ p_{|102\rangle}(t) \\ p_{|020\rangle}(t) \\ p_{|101\rangle}(t) \\ \rho_{\text{coh}}(t) \end{pmatrix} = R_{\text{P}} \begin{pmatrix} p_{|000\rangle}(t) \\ p_{|100\rangle}(t) \\ p_{|010\rangle}(t) \\ p_{|001\rangle}(t) \\ p_{|002\rangle}(t) \\ p_{|102\rangle}(t) \\ p_{|020\rangle}(t) \\ p_{|101\rangle}(t) \\ \rho_{\text{coh}}(t) \end{pmatrix}. \tag{S6}$$

The rate matrix R_{P} is defined as

$$R_{\text{P}} \coloneqq \begin{pmatrix} -\Gamma_{1\uparrow} + \Gamma_{2\uparrow} + \Gamma_{3\uparrow} & \Gamma_{1\downarrow} & \Gamma_{2\downarrow} & \Gamma_{3\downarrow} & 0 & 0 & 0 & 0 & 0 \\ \Gamma_{1\uparrow} & -(\Gamma_{1\downarrow} + \Gamma_{3\uparrow}) & 0 & 0 & 0 & 0 & 0 & \Gamma_{3\downarrow} & 0 \\ \Gamma_{2\uparrow} & 0 & -(\Gamma_{2\downarrow} + 2\Gamma_{2\uparrow}) & 0 & 0 & 0 & 2\Gamma_{2\downarrow} & 0 & 0 \\ \Gamma_{3\uparrow} & 0 & 0 & -(\Gamma_{3\downarrow} + \Gamma_{1\uparrow} + 2\Gamma_{3f\uparrow}) & 2\Gamma_{3f\downarrow} & 0 & 0 & \Gamma_{1\downarrow} & 0 \\ 0 & 0 & 0 & 2\Gamma_{3f\uparrow} & -(\Gamma_{1\uparrow} + 2\Gamma_{3f\downarrow}) & \Gamma_{1\downarrow} & 0 & 0 & 0 \\ 0 & 0 & 0 & 0 & \Gamma_{1\uparrow} & -(\Gamma_{1\downarrow} + 2\Gamma_{3f\downarrow}) & 0 & 2\Gamma_{3f\uparrow} & 0 \\ 0 & 0 & 2\Gamma_{2\uparrow} & 0 & 0 & 0 & -2\Gamma_{2\downarrow} & 0 & 2A \\ 0 & \Gamma_{3\uparrow} & 0 & \Gamma_{1\uparrow} & 0 & 2\Gamma_{3f\downarrow} & 0 & -(\Gamma_{1\downarrow} + \Gamma_{3\downarrow} + 2\Gamma_{3f\uparrow}) & -2A \\ 0 & 0 & 0 & 0 & 0 & 0 & -A & A & \Gamma_{\text{C}} \end{pmatrix} \tag{S7}$$

We define the Γ's as follows. Denote by n_i the average number of synthesized quasithermal photons in the waveguide coupled to qudit Q_i; and, by $n_{i,\text{res}}$, the average number of native thermal (i.e., residual) photons already present in waveguide $i = 1, 2$. $n_{3,\mathrm{res}}$ is the effective average number of photons that populate qudit Q_3's environment and that affect Q_3's *first transition*, $|000\rangle \leftrightarrow |001\rangle$. We also introduce $n_{3f,\mathrm{res}}$ as the average number of photons affecting the Q_3's *second transition*, $|001\rangle \leftrightarrow |002\rangle$. In terms of these quantities, we define lowering rates $\Gamma_{i\downarrow} = \Gamma_i(n_i + n_{i,\mathrm{res}} + 1)$ and raising rates $\Gamma_{i\uparrow} = \Gamma_i(n_i + n_{i,\mathrm{res}})$ for qudits $i \in \{1, 2\}$, as well as $\Gamma_{3\downarrow} = \Gamma_{\mathrm{E}}(n_{3,\mathrm{res}} + 1)$ and $\Gamma_{3\uparrow} = \Gamma_{\mathrm{E}} n_{3,\mathrm{res}}$. Similarly, $\Gamma_{3f\uparrow} = \Gamma_{\mathrm{E}} n_{3f,\mathrm{res}}$ and $\Gamma_{3f\downarrow} = \Gamma_{\mathrm{E}}(n_{3f,\mathrm{res}} + 1)$ denote the analogous rates at the frequency of Q_3's second transition ($|001\rangle \leftrightarrow |002\rangle$). For brevity, Eq. (S7) also contains a new notation Γ_{C} defined as $\Gamma_{\mathrm{C}} = -(2\Gamma_{2\downarrow} + 2\Gamma_{2\uparrow} + \Gamma_{1\downarrow} + \Gamma_{1\uparrow} + \Gamma_{3\downarrow} + \Gamma_{3\uparrow})/4$.

To model the data in Figs. 3b, 4a and 4b, we solve Eq. (S6) with the initial condition

$$(p_{|000\rangle}(0), p_{|100\rangle}(0), p_{|010\rangle}(0), p_{|001\rangle}(0), p_{|002\rangle}(0), p_{|102\rangle}(0), p_{|020\rangle}(0), p_{|101\rangle}(0), \rho_{\mathrm{coh}}(0)) \\ = (0.028, 0.003, 0.007, 1 - 0.028 - 0.0008, 0.0008, 0, 0, 0, 0). \quad \text{(S8)}$$

This vector represents the state prepared before the refrigeration—the state that the system is in after the π-pulse that impacts Q_3's 0–1 transition (see Fig. 3b in the main text). Before the π-pulse, the Q_3 states $|1\rangle$ and $|2\rangle$ contain residual populations of 0.028 (experimentally determined) and $0.028^2 = 0.0008$, respectively. We estimate Q_3's $|2\rangle$ population under two assumptions: First, Q_3's environment acts as a bath with the effective temperature T_{E}. This temperature is the same for both the transitions, $|0\rangle \leftrightarrow |1\rangle$ and $|1\rangle \leftrightarrow |2\rangle$. Second, Boltzmann factors determine the detailed-balance rate for both these transitions. Therefore, $P_1 = P_0 \exp[-\hbar\omega_3/(k_{\mathrm{B}}T_{\mathrm{E}})]$, and $P_2 = P_1 \exp[-\hbar(\omega_3 + \alpha_3)/(k_{\mathrm{B}}T_{\mathrm{E}})] = P_0 \exp[-\hbar(2\omega_3 + \alpha_3)/(k_{\mathrm{B}}T_{\mathrm{E}})] \approx \{\exp[-\hbar\omega_3/(k_{\mathrm{B}}T_{\mathrm{E}})]\}^2$. The last approximation is justified because $\alpha_3 \ll 2\omega_3$. Our assumption would have been undermined if two-level fluctuators were in Q_3's environment, which could lead to widely different T_{E} across short frequency ranges [4]. However, we have observed that our measured P_{res} does not lie outside a fixed narrow range (see Sec. VII below) across thermal cyclings of the device. This observation supports our assumption that T_{E} is uniform across small frequency ranges. Thus, Q_3's $|0\rangle$ level has a population $1 - 0.028 - 0.0008$. The populations of Q_1's state $|1\rangle$ is 0.003. The populations of Q_2's level $|1\rangle$ is 0.007. The aforementioned π-pulse exchanges the populations of the Q_3 levels $|0\rangle$ and $|1\rangle$, yielding the vector (S8).

Having introduced our dynamical model, we review the steady-state coefficient of performance (COP), following Ref. [5]. Denote by $\mathcal{J}_T$ the steady-state current of heat drawn from the target system. Denote by $\mathcal{J}_H$ the steady-state current of heat drawn by Q_1 from the hot bath. The currents' ratio equals an absorption refrigerator's steady-state COP:

$$\mathrm{COP} := \mathcal{J}_T / \mathcal{J}_H \,. \quad \text{(S9)}$$

The steady-state heat current drawn from bath $i \in \{1, 2, 3\}$ is

$$\mathcal{J}_i = \mathrm{Tr}(\hat{H} \mathcal{L}_i \rho(\infty)). \quad \text{(S10)}$$

The Lindbladian therein acts as $\mathcal{L}_i \hat{\rho} = \Gamma_i \left\{ (n_i + n_{i,\mathrm{res}} + 1)\, \mathcal{D}[\hat{\hat{a}}_i, \hat{\rho}] + (n_i + n_{i,\mathrm{res}}) \mathcal{D}[\hat{\hat{a}}_i^\dagger, \hat{\rho}] \right\}$.

III. RABI POPULATION-MEASUREMENT SCHEME

Figure S2 shows the pulse sequence used to measure Q_3's level-$|1\rangle$ population more accurately than standard qubit readout allows [6, 7]. This Rabi scheme involves the Q_3 energy levels $|0\rangle$, $|1\rangle$, and $|2\rangle$. We measure the qubit-state readout in the subspace $\mathrm{span}\{|1\rangle, |2\rangle\}$. The measured readout voltage can be expressed as

$$S = S_0 P_0 + S_1 P_1 + S_2 P_2. \quad \text{(S11)}$$

P_i denotes the population of Q_3's i^{th} state, for $i \in \{0, 1, 2\}$. S_i represents the respective weighted coefficient. In the main text, we present the excited-state population, $P_1 + P_2$, as P_{exc}.

The scheme for measuring Q_3's excited-state population involves two different Rabi oscillations. We drive Rabi oscillations between $|1\rangle$ and $|2\rangle$ in each of two cases: with and without a prior π-pulse in the subspace $\mathrm{span}\{|0\rangle, |1\rangle\}$. The prior pulse interchanges the populations of $|0\rangle$ and $|1\rangle$, i.e., interchanges P_0 and P_1 (see the 0–1 pulse with the dashed outline in Fig. S2a). We measure and denote these Rabi oscillations' amplitudes by S_{R} (the Reference in Fig. S2c) and S_{S} (the Signal in Fig. S2c), respectively. We determine S_{R} and S_{S}, while saving experiment runtime as follows: We perform a two-point measurement at $\theta = 0$ and $\theta = \pi$, to determine the amplitudes of the Rabi oscillations. From those measurements, we compute a ratio S_{P} related to the populations P_1 and P_2:

$$S_{\mathrm{P}} = \frac{S_{\mathrm{S}}}{S_{\mathrm{S}} + S_{\mathrm{R}}} = \frac{P_1 - P_2}{1 - 3P_2} \approx P_1 - P_2 \quad \text{(S12)}$$

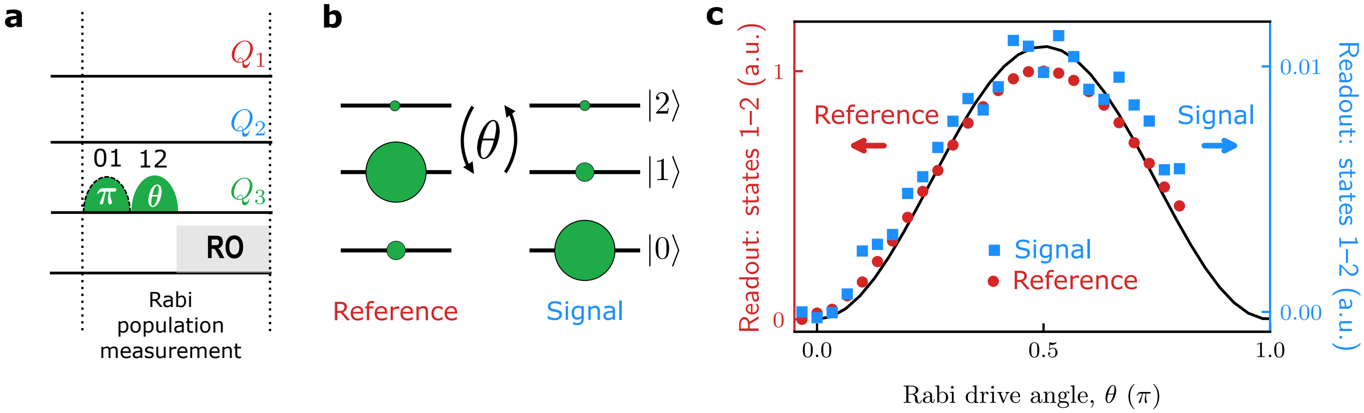

FIG. S2: Rabi measurement of the population in qubit Q_3's $|1\rangle$ level. (a) Pulse sequence for the scheme. The notation 0–1 (1–2) indicates that the pulse drives the transition $|0\rangle \leftrightarrow |1\rangle$ ($|1\rangle \leftrightarrow |2\rangle$). θ denotes the pulse drive's Rabi angle. The pulse with the dashed outline is present in the reference measurement and absent from the signal measurement. The readout (RO) is performed in the subspace span$\{|1\rangle, |2\rangle\}$. (b) Representation of the relative distribution of populations across qubit Q_3's $|0\rangle$, $|1\rangle$, and $|2\rangle$ levels when Q_3 is in its natural steady-state. (c) Rabi oscillations. The Rabi oscillation resulting from the 1–2 pulse after the 0–1 pulse provides a reference trace (red). The Rabi oscillation produced without the 1–2 pulse provides the signal—the actual population trace (blue).

The last approximation holds if $P_2 \ll 1$.

Importantly, refrigeration with a large n_{H} results in a population P_1 that is very low ($\lesssim 0.001$) and is comparable to P_2. Our scheme cannot separate these two populations' contributions to the measured S_{P}. Nonetheless, our quantitative 8-level model can yield a theoretical P_2, which is multiplied by 2 and added to our measured S_{P} value. Thus, we obtain the excited-state population: $P_{\mathrm{exc}} = P_1 + P_2$. The result agrees with the calculation (Fig. S3).

IV. POPULATION MEASUREMENTS NEAR NOISE FLOOR

Our population measurement is particularly challenging when the population reaches very low values—specifically below 0.001, which appears to be the noise floor of our population measurements in Fig. 3b. Given this experimental limitation, we interpret the data near this noise floor with special consideration and draw conservative conclusions. Our measurements near the noise floor also yield negative values sometimes, as reported in [7, 8]. The noise floor stems from the susceptibility of our measurement technique, which involves voltage-readout signals, to stochastic voltage noise in the measurement circuit—noise sourced predominantly by the circuit's amplifiers (see Fig. S1).

We make a conservative estimate of the noise floor of our population measurements, shown in the main text's Fig. 3b, as follows. We consider three representative datasets for which $n_{\mathrm{H}} > 1$. We analyze fluctuations for values of time duration $\Delta t > 40$ μs. Here, our measurements appear close to or have reached the noise floor. Furthermore, the theoretical curves modelling the data relatively well, especially at low Δt, also indicate that the populations have reached their steady-state values for $\Delta t > 40$ μs . We compute the standard deviation for each curve separately, for $\Delta t > 40$ μs, yielding three estimates of the uncertainty in our measurements. We regard their average as the uncertainty in our measurements, $\sigma = 0.0004$. We identify the noise floor as $2\sigma = 0.0008$ above zero; it is shaded in gray in Fig. 3b.

We perform a similar analysis to extract the value of, and uncertainty in, P_{SS} when it reaches its lowest value by refrigeration. Specifically, we analyze the experimental curve for P_{SS} as a function of n_{H}, at the lowest $n_{\mathrm{C}} = 0.007$ (left plot of Fig. 4a). We acquired this dataset separately from the other three curves in Fig. 4a: We achieved a better signal-to-noise ratio (with more ensemble averaging and better qubit-readout settings), which is critical when P_{SS} is near the noise floor. We evaluate the lowest P_{SS} by computing the mean of the measured values of the curve that have declined below 0.0008 (an estimate of the noise floor identified above and depicted in Fig. 3b). This is a conservative evaluation of the mean. We are likely over-estimating the value of lowest P_{SS}, thereby underestimating our refrigerator's capability. We estimate the uncertainty by computing the standard deviation of the same set of values of P_{SS}. In conclusion, the mean and standard deviation are 3×10^{-4} and 2×10^{-4}, respectively. A similar procedure was applied for other experimental curves in Fig. 4a to determine the uncertainty. For those curves, the standard deviation is 5×10^{-4}

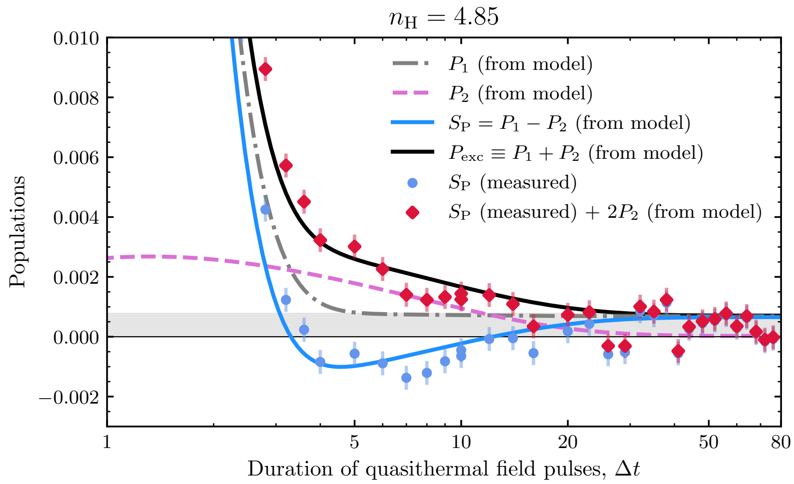

FIG. S3: Measured and calculated populations as functions of the time duration Δt of the applied quasithermal fields, with $n_{\mathrm{H}} = 4.85$. This is one of the datasets presented in the main text's Fig. 3b. Recall that P_1 and P_2 denote the populations of Q_1's $|1\rangle$ and $|2\rangle$ levels. These populations are calculated from the 8-level population-rate model in Eq. S6, presented in Sec. II. The experimentally inferred ratio S_{P} is related to the levels' populations as $P_1 - P_2$. The measured data (blue circles) is compared to the blue curve calculated theoretically. From the measured S_{P} and calculated P_2, we obtain the excited-state population: $P_{\mathrm{exc}} = S_{\mathrm{P}} + 2P_2$ (cross-data points). This result is compared with the corresponding theoretical (black) curve, which represents $P_1 + P_2$. The error bars represent the standard deviations about the mean values, represented by symbols (see Sec. IV for method). The shaded area represents estimate of the measurement's noise floor (see Sec. IV for method). Accounting for P_2 is particularly important when P_{exc} reaches near 0.001 at intermediate Δt values, when P_1 may become comparable to P_2. P_2 rises at intermediate Δt because of the population transfer from the Q_3's state $|1\rangle$ to state $|2\rangle$ at rate $2\Gamma_{3fu}$ (see the rate equation in sec. II above). This process is impeded by the competing refrigeration process transferring population from state $|1\rangle$ to state $|0\rangle$ instead. At both low and high Δt values, P_2 is negligible compared to P_1.

V. ENGINEERING GUIDELINES

The main parameters usable to engineer our quantum refrigerator are the transition frequencies ω_1, ω_2, and ω_3; the dissipation rates Γ_1 and Γ_2; and the three-body-interaction strength A. The interaction exchanges $|101\rangle$ and $|020\rangle$ only when the transition frequencies satisfy the resonance condition,

$$\omega_1 + \omega_3 = 2\omega_2 + \alpha_2. \tag{S13}$$

The greater the A, the more quickly our quantum refrigerator can cool the target qubit. In the perturbative approximation (when $g_{12}, g_{23} \ll \omega_1, \omega_2, \omega_3$), A has the form [1]

$$A = \sqrt{2}\, g_{12}\, g_{23} \left(\frac{1}{2\omega_2 + \alpha_2 - \omega_1} + \frac{1}{2\omega_2 + \alpha_2 - \omega_3} \right). \tag{S14}$$

$A/(2\pi)$ is limited to values on the order of few MHz, for the nominal parameter values of $g_{12}, g_{23}, \omega_1, \omega_2, \omega_3$, within the applicability of the full Hamiltonian's rotating-wave approximation. Our quantum refrigerator has two steady-state metrics: the target's steady-state temperature, T_{SS}, and the steady-state COP. We expect the generic quantum-absorption-refrigerator model [9] to describe our quantum refrigerator. It implies

$$T_{\mathrm{SS}} = \frac{2\omega_2 + \alpha_2 - \omega_1}{(2\omega_2 + \alpha_2)/T_{\mathrm{C}} - \omega_1/T_{\mathrm{H}}}. \tag{S15}$$

This result relies on the assumption that the target qubit couples to its environment only weakly (at a low rate Γ_{E}).

High T_{H} values (high n_{H} values) favor low T_{SS} values. A high n_{H} populates the Q_1's level $|1\rangle$ more: Q_1 becomes excited at a rate $n_{\mathrm{H}}\Gamma_1$ and de-excites at a rate $(n_{\mathrm{H}}+1)\Gamma_1$. Thus, Q_1's $|1\rangle$ level achieves its greatest population when n_{H} is large. When Q_1's $|1\rangle$ is highly populated, $|101\rangle$ is highly populated. This condition is the precursor to the cooling via the cascade process $|101\rangle \to |020\rangle \to |010\rangle$.

For a different reason, low T_{C} values (low n_{C} values) favor low T_{SS} values. The levels $|020\rangle$ and $|010\rangle$ have low populations. The reverse process $|010\rangle \to |020\rangle \to |101\rangle$, which undermines the refrigeration, is therefore suppressed.

For the sake of analyzing the refrigerator's dynamics, we model with an exponential function the decay of Q_3's excited-state population, $P_{\rm exc}$, as a function of the duration Δt for which the quasithermal fields are applied (see Fig 3b). The exponential approximation appears reasonable from our measurements, particularly until $P_{\rm exc}$ has declined to 0.01. We denote the cooling rate of Q_3 by $\Gamma_{\rm cool}$. $\Gamma_{\rm cool}$ is closely related to the inverse of reset time shown in Fig. 4b (the time needed for Q_3's excited-state population to reach 0.01). In the optimization of $\Gamma_{\rm cool}$, the dissipation rates (Γ_1 and Γ_2) and A play a critical role. Specifically, under the conditions $n_{\rm H} \gg 1$ and $n_{\rm C} \ll 1$, $n_{\rm H}\Gamma_1$ ($= \Gamma_{1\uparrow} \approx \Gamma_{1\downarrow}$) and Γ_2 ($\approx \Gamma_{2\downarrow}$) are the relevant rates. If these rates are too small, they become the limiting factors in the cascade process $|001\rangle \to |101\rangle \to |020\rangle \to |010\rangle$ that effects the refrigeration. On the other hand, if those rates are too high, the three-body coherent-exchange process suffers excessive dephasing and becomes the limiting factor. Figure S4 shows a 2D plot of $\Gamma_{\rm cool}/A$ as a function of $n_{\rm H}\Gamma_1/A$ and Γ_2/A, calculated from our 8-level population model. Optimal values of $n_{\rm H}\Gamma_1/A$ and Γ_2/A maximize $\Gamma_{\rm cool}$. Our experimental parameters fall at the gray cross-hair in Fig. S4. The maximum $\Gamma_{\rm cool}$ corresponds to a minimum in reset (the time taken to reach $P_{\rm exc} = 0.01$). That is, Fig. S4 guides the choice of parameters used to further reduce the reset time, as illustrated in Fig. 4b of the main text. A simpler version of the model, containing only 3 levels ($|001\rangle$, $|101\rangle$, and $|020\rangle$), yields the optimal values of the parameters close to that of the 8-level model. Thus, this simpler model suffices for engineering the refrigerator. However, the 3-level model does not fit our main results quantitatively.

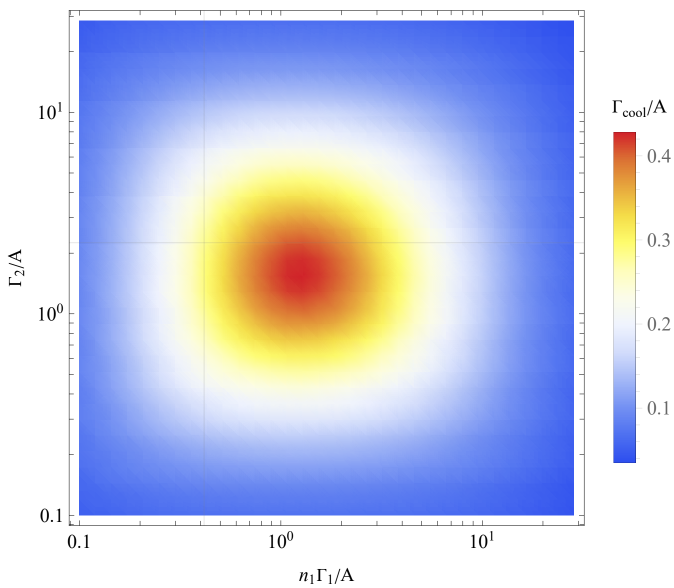

FIG. S4: Two-dimensional plot of $\Gamma_{\rm cool}/A$ as a function of $n_{\rm H}\Gamma_1/A$ and Γ_2/A, calculated from our 8-level model. $\Gamma_{\rm cool}$ is defined as the rate of the decay of Q_3's excited-state population to 0.01. The cross-hair indicates our experimentally realized values: $n_{\rm H} = 19.4$, $\Gamma_1/(2\pi) = 70$ kHz, $\Gamma_2/(2\pi) = 7.2$ MHz, and $A/(2\pi) = 3.2$ MHz. The experimentally determined $\Gamma_{\rm cool}/(2\pi) = 0.69$ MHz, which is close to the calculated $\Gamma_{\rm cool}/(2\pi) = 0.9$ MHz.

VI. REFRIGERATION'S DEPENDENCE ON COLD-BATH TEMPERATURE

Figure S5 shows the Q_3's excited-state population, $P_{\rm exc}$, as a function of the duration Δt for which the quasithermal microwave modes are applied. We present these data at several values of the average number $n_{\rm C}$ of photons in the cold bath. The average number $n_{\rm H}$ of hot-bath thermal photons is a high value, 35.

Increasing $n_{\rm C}$ populates Q_2's excited states incoherently, rendering the qutrit's state mixed [10]. The mixing hinders the three-body process $|101\rangle \to |020\rangle$. The refrigeration is impeded, so the steady-state $P_{\rm exc}$ increases.

VII. REFRIGERATION OF Q_3 INITIATED IN ITS NATURAL STEADY STATE

In this study, we begin with Q_3 in the steady state that results from Q_3's equilibrating as much as possible with its environment. (The state may, in fact, be far from equilibrium.) According to our measurements, Q_3's $|1\rangle$ level has a population $P_{\rm exc}$ of 0.028 in this state. We allow our quantum refrigerator to run for a duration Δt. Then, we

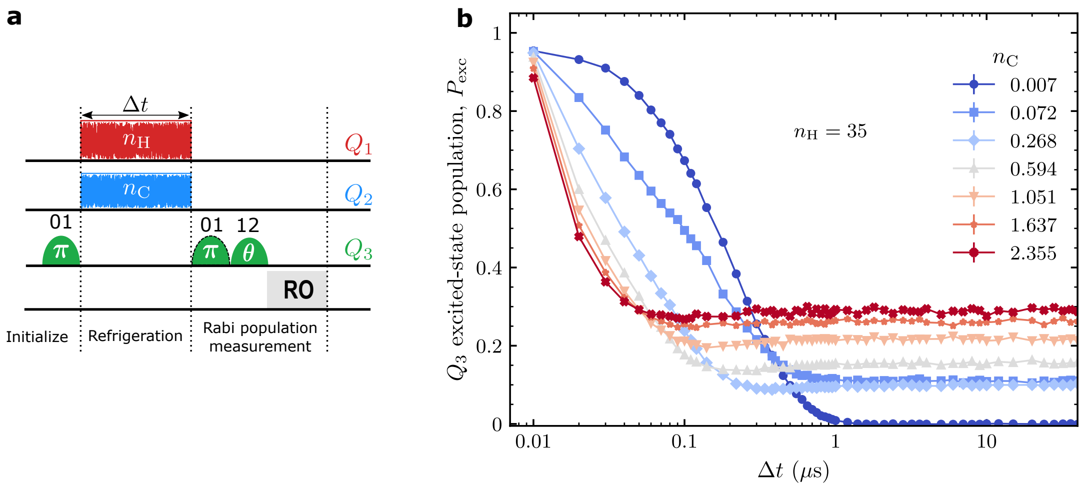

FIG. S5: Refrigeration's dependence on cold-bath temperature. (a) Pulse scheme. (b) Q_3's excited-state population, P_exc, as a function of the time duration Δt of the application of quasithermal field, at select values of the average number n_C of thermal photons in the cold bath. The average number n_H of photons fixed at the high value 35.

perform a Rabi population measurement of $|1\rangle$. (See the pulse scheme in Fig. S4a.) P_exc is plotted as a function of Δt in Fig. S4. Here, P_exc begins at a much lesser value than in the main text's Fig. 3b. Therefore, P_exc reaches its long-time value, here, by an earlier time ≈ 800 ns.

We observed that P_res varied between 0.015 and 0.028 across long time frames (days) during the experiments. Such a large P_res (which is the motivation for reset) originates from uncontrolled non-equilibrium processes, such as stray infrared-radiation and inadequate device thermalization. Minute changes in the strength of these uncontrolled processes could lead to such changes in P_res.

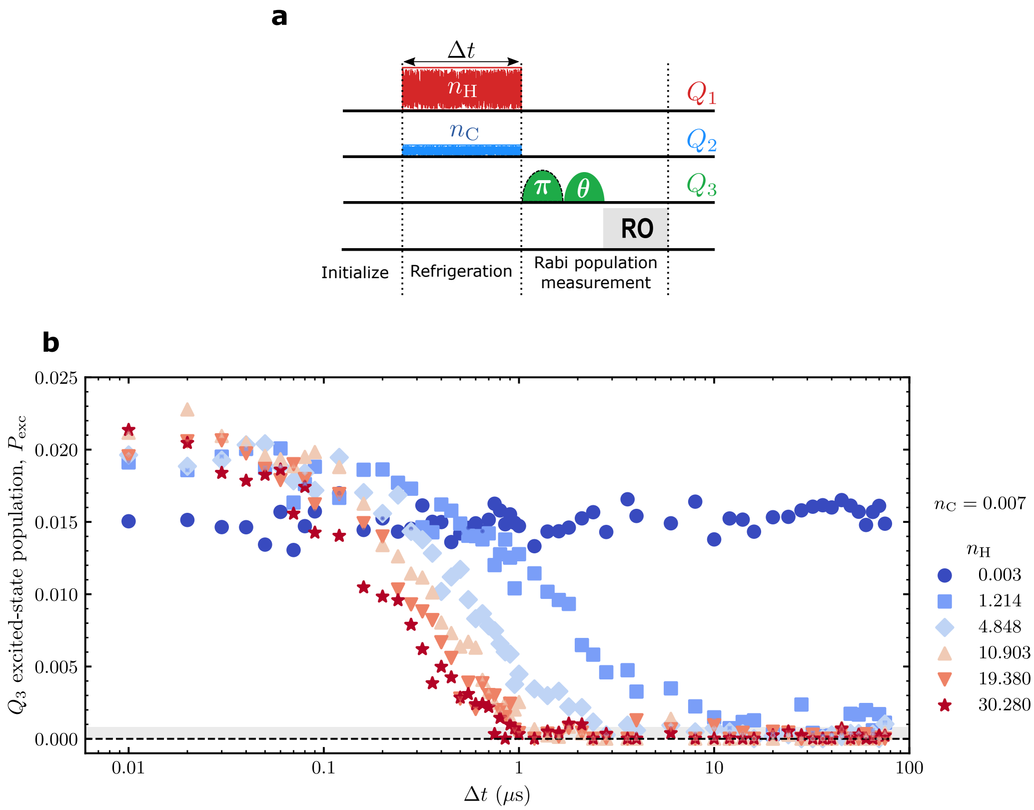

FIG. S6: Refrigeration of target qubit initialized with a residual $|1\rangle$ population of 0.020. (a) Pulse scheme. The qubit is not initialized entirely in the excited state. (b) Q_3's excited-state population, P_exc, as a function of the time duration Δt of the thermal-microwave-mode pulse, for select values of the average number n_H of thermal photons in the hot bath.

[1] W. Ren, W. Liu, C. Song, H. Li, Q. Guo, Z. Wang, D. Zheng, G. S. Agarwal, M. O. Scully, S.-Y. Zhu, H. Wang, and D.-W. Wang, Simultaneous Excitation of Two Noninteracting Atoms with Time-Frequency Correlated Photon Pairs in a Superconducting Circuit, Physical Review Letters **125**, 133601 (2020).

[2] S. E. Nigg, H. Paik, B. Vlastakis, G. Kirchmair, S. Shankar, L. Frunzio, M. H. Devoret, R. J. Schoelkopf, and S. M. Girvin, Black-Box Superconducting Circuit Quantization, Phys. Rev. Lett. **108**, 240502 (2012).

[3] H. J. Carmichael and D. F. Walls, Master equation for strongly interacting systems, Journal of Physics A: Mathematical, Nuclear and General **6**, 1552 (1973).

[4] A. Kulikov, R. Navarathna, and A. Fedorov, Measuring Effective Temperatures of Qubits Using Correlations, Phys. Rev. Lett. **124**, 240501 (2020).

[5] P. P. Hofer, M. Perarnau-Llobet, J. B. Brask, R. Silva, M. Huber, and N. Brunner, Autonomous quantum refrigerator in a circuit QED architecture based on a Josephson junction, Phys. Rev. B **94**, 235420 (2016).

[6] K. Geerlings, Z. Leghtas, I. M. Pop, S. Shankar, L. Frunzio, R. J. Schoelkopf, M. Mirrahimi, and M. H. Devoret, Demonstrating a Driven Reset Protocol for a Superconducting Qubit, Phys. Rev. Lett. **110**, 120501 (2013).

[7] X. Y. Jin, A. Kamal, A. P. Sears, T. Gudmundsen, D. Hover, J. Miloxi, R. Slattery, F. Yan, J. Yoder, T. P. Orlando, S. Gustavsson, and W. D. Oliver, Thermal and Residual Excited-State Population in a 3D Transmon Qubit, Physical Review Letters **114**, 240501 (2015).

[8] Y. Zhou, Z. Zhang, Z. Yin, S. Huai, X. Gu, X. Xu, J. Allcock, F. Liu, G. Xi, Q. Yu, H. Zhang, M. Zhang, H. Li, X. Song, Z. Wang, D. Zheng, S. An, Y. Zheng, and S. Zhang, Rapid and Unconditional Parametric Reset Protocol for Tunable Superconducting Qubits, Nature Communications **12**, 5924 (2021).

[9] M. T. Mitchison, Quantum thermal absorption machines: Refrigerators, engines and clocks, Contemporary Physics **60**, 164 (2019).

[10] M. Scigliuzzo, A. Bengtsson, J.-C. Besse, A. Wallraff, P. Delsing, and S. Gasparinetti, Primary Thermometry of Propagating Microwaves in the Quantum Regime, Physical Review X **10**, 041054 (2020).